Available online at www.sciencedirect.com

ScienceDirect

Journal of the European Ceramic Society 35 (2015) 585–595

www.elsevier.com/locate/jeurceramsoc

Dispersion, connectivity and tortuosity of hierarchical porosity composite SOFC cathodes prepared by freeze-casting

A.Z. Lichtner [a], D. Jauffrès [b], D. Roussel [b], F. Charlot [c], C.L. Martin [b], R.K. Bordia [a,*]

[a] *Department of Materials Science and Engineering, University of Washington, Roberts Hall, Box 352120, Seattle, WA 98195, United States*
[b] *University Grenoble Alpes, CNRS, SIMAP, F-38000 Grenoble, France*
[c] *Grenoble-INP, CMTC, BP 46 38402 Saint Martin d'Hères Cedex, France*

Received 13 April 2014; received in revised form 16 September 2014; accepted 21 September 2014
Available online 2 October 2014

Abstract

Aqueous co-dispersions of Lanthanum Strontium Manganite (LSM) and Yttria-Stabilized Zirconia (YSZ) were freeze-cast and partially sintered, resulting in anisotropic, hierarchically porous composites for potential applications as solid oxide fuel cell (SOFC) cathodes. The uniform phase dispersion was validated using SEM–EDS and FIB-SEM tomography. Using reconstructed 3D images of samples sintered at 1200 and 1300 °C, the effect of sintering on phase connectivity, triple phase boundary (TPB) density and phase tortuosity was explored. The higher sintering temperature resulted in lower TPB density and, less open pore volume but decreased tortuosity for both the LSM and YSZ due to densification of the structure at high temperatures. Due to the unique double-sided morphology of the freeze-cast walls and the benefits gained from less tortuous percolation paths, a decrease in TPB density and open porosity from elevated sintering temperatures may not degrade the electrochemical performance as much as it would for a standard isotropic microstructure.

Keywords: SOFC; Hierarchical porosity; 3D microstructure; TPB; Freeze-casting

1. Introduction

Solid oxide fuel cells (SOFC) are electrochemical devices used to efficiently convert chemical energy from a fuel (e.g. H_2) into electrical energy. An SOFC typically is comprised of a dense electrolyte and two porous composite electrodes. Electrochemical reactions take place within the composite electrodes at the so-called triple phase boundary (TPB) where the gas (porous phase), ionic conductor and electronic conductor meet. To function, the porous phase must be connected to a gas inlet, the ionic conductor should be connected to the electrolyte and the electron conductor should connect with the current collector and external circuit. A high operating temperature (typically between 600 and 1000 °C) is needed to ensure adequate ionic conductivity within the ion-conducting material, usually Yttria-Stabilized Zirconia (YSZ). The most common materials used for the electron conductor are Strontium-Doped Lanthanum Manganite (LSM) for the cathode and nickel metal for the anode.

Powder processing techniques such as tape-casting or screen-printing followed by partial sintering are commonly used methods for obtaining SOFC electrodes which maintain sufficient porosity for gas access.[1] The microstructure of the electrodes plays a crucial role in the performance of the SOFC, and its optimization is a complex process due to the following functional requirements: (1) ensure high electronic and ionic conductivity, (2) maximize total TPB density and (3) maximize gas access to the TPBs by maintaining adequate open porosity. In addition, handling and thermal loading require that the electrodes maintain a minimum amount of strength and toughness.

It is worth noting that some of these requirements are contradictory; for example, gas access can be easily improved by increasing porosity but this results in a decrease in conductivity and strength. The development of new microstructures and their careful characterization combined with modeling approaches

* Corresponding author at: Department of Materials Science and Engineering, Clemson University, 161 Sirrine Hall, Clemson, SC 29634, United States. Tel.: +1 864 656 5228; fax: +1 864 656 5973.
E-mail address: rbordia@clemson.edu (R.K. Bordia).

http://dx.doi.org/10.1016/j.jeurceramsoc.2014.09.030
0955-2219/

is a promising way of obtaining tailored microstructures with an optimal compromise between the various electrode properties. In this respect, anisotropic structures offer an interesting alternative to isotropic ones. Indeed, some of the requirements mentioned above are actually directional, namely conductivity, gas access and to a certain extent mechanical properties. The freeze-casting process in particular can be used to obtain a microstructure with aligned pore channels to improve gas penetration and aligned walls to provide enhanced mechanical properties. This process takes advantage of the highly directional growth of ice crystals within a ceramic slurry followed by removal of the ice crystals by sublimation to controllably template a directionally porous ceramic.[2,3] The green body can then be partially sintered to obtain a hierarchical structure with aligned macro-pores (~10–20 μm) that alternate with microporous ceramic walls. In the previous few years, freeze-casted composite anodes have been produced by several research groups,[4–6] but only recently, the successful processing of freeze-cast LSM–YSZ cathode materials has been reported.[7]

Within the context of freeze-cast processing as a means of microstructure tailoring, studying the influence of processing parameters on the microstructure of the ceramic walls is essential. Indeed, the electrochemical performance of a freeze-cast electrode is highly dependent on the microstructure of its walls, which is controlled by the sintering temperature, freezing conditions and initial slurry characteristics (composition, particle size, dispersion, etc.).[2] In particular, an essential requirement to obtain a functioning composite electrode is the percolation of both the ionic and electronic conducting materials. This requirement can be met using a properly dispersed composite suspension. If both the ionic and electronic conductors have the same particle size and conductivity, the ideal volume ratio for maximum electrochemical performance would be 50:50. Since however, the conductivity of YSZ is over 100 times slower than that of LSM, a 40:60 volume ratio of LSM:YSZ has been shown to increase performance by decreasing ohmic losses while still maintaining percolation of both the electron- and ion-conducting networks.[8,9]

The microstructures of these directionally porous, hierarchical ceramics has been investigated using Focused Ion Beam-Scanning Electron Microscope (FIB-SEM) tomography, which is based on the serial sectioning by FIB and SEM imaging of a sample followed by reconstruction of the SEM micrographs into a 3D image. This powerful technique allows the quantitative 3D examination of electrode microstructures and has been used to study the influence on electrode performance of electrode composition,[10,11] sintering temperature[12] and particle size.[13]

The objective of the present study is to develop a co-dispersion procedure for LSM and YSZ to make a slurry that can be freeze-cast, validate the phase dispersion, characterize the structure of freeze-cast SOFC cathode material, and to analyze the effect of sintering temperature on the microstructure of the microporous walls. First, the spatial dispersion and phase composition of the LSM and YSZ phases are investigated using Scanning Electron Microscopy (SEM), Energy Dispersive Spectroscopy (EDS) and X-ray Diffractometry (XRD). Then FIB-SEM tomography is used to investigate the microstructure at the scale of a single wall (~15 μm) from two LSM–YSZ freeze-casts sintered at two different temperatures (1200 and 1300 °C). These temperatures were chosen as they gave significantly different micro-pore morphologies while still maintaining adequate strength and residual porosity for use as an SOFC cathode. FIB-SEM characterization was used to confirm the proper spatial repartition of LSM and YSZ grains and to analyze the effect of the sintering temperature on the connectivity of the LSM, YSZ and pore phases within the walls of a freeze-cast SOFC cathode. FIB-SEM characterization also allows the density of TPBs as well as the tortuosity factors for all three phase networks (LSM, YSZ and pores) to be calculated in various directions.

2. Experimental procedure

2.1. Preliminary aqueous co-dispersion studies

Initial attempts at slurry dispersion and freeze-casting were based on previously successful methods for co-dispersing SOFC anode materials.[14] The LSM and YSZ powders were first ball-milled dry to form a homogenous powder. This mixture was slowly added into deionized (DI) water containing an ammonium polymethacrylate dispersant (Darvan C-N, R.T. Vanderbilt Co., Norwalk, CT) until approximately 25 vol.% solids was reached. The pH was not controlled during these initial attempts. The slurries produced using this method were highly viscous and impossible to freeze-cast no matter the level of dispersant used.

More advanced, methods for the co-dispersion of two materials typically rely on exploiting the isoelectric points of the individual materials.[15] These methods alone proved inadequate however and the suspensions which were initially created were unstable and resulted in the immediate segregation of LSM from YSZ. Indeed, over a broad range of experimental parameters (18–25 vol.% solids, 1.5–5 wt.% dispersant, 3–5 wt.% binder, pH = 6–10), freeze-casting resulted in the formation of spherical YSZ agglomerates, which sintered into dense spheres 10–50 μm in size, which would embed themselves within the larger freeze-cast matrix (Fig. 1). EDS spectra showed that these spheres were composed almost exclusively of YSZ. The spheres reduced the active volume fraction of YSZ within the freeze-cast matrix inhibiting the percolation of the ion-conducting phase.

Three steps were required to produce a stable, aqueous co-dispersion. First, YSZ must be fully dispersed on its own, prior to the addition of the LSM, thereby allowing full coverage of the dispersant on the YSZ particles. Second, the pH of the solution during co-dispersion must be carefully controlled. Acidic pH values can potentially lead to the leaching of Yttrium ions out of solution while values too close to the isoelectric points of the materials (6 and 8 for LSM and YSZ, respectively) will result in particle sedimentation.[16–18] For these reasons, the pH of the slurry was kept between 7 and 8. At this pH, the two particles are oppositely charged and coagulate without segregation. Lastly, the viscosity of the slurry must remain high enough to partially coagulate the suspension, hindering the majority of particle segregation, while at the same time be low enough to still allow the slurry to be easily freeze-cast.[7] The high

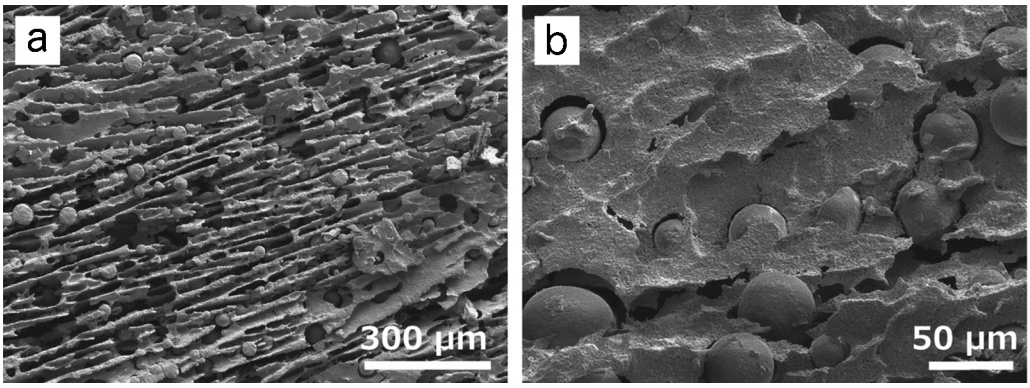

Fig. 1. Overview (a) and magnified (b) SEM micrographs of the LSM-YSZ structure containing dense, embedded YSZ-spheres that formed spontaneously in response to non-ideal dispersion conditions. Samples were partially sintered to 1200 °C before being sectioned and imaged.

viscosity and the coagulated nature of the slurry led to a condition in which segregation does not occur. For the LSM–YSZ system, the range of usable dispersants was found to be between 1.6 and 2.4 wt.% of the solids, and though these values appear high, they were found to be the necessary levels of dispersant for this particular system. Once formed, these slurries are highly stable, often lasting many days without appreciable degradation.

2.2. Optimized electrode preparation

A 23 vol.% (61.5 wt.%) solids ceramic suspension was prepared by mixing DI-water with a small amount (1.6 wt.%) of Darvan C-N at neutral pH. The solution was stirred for 20 min to ensure complete dissolution of the dispersant. The pH of the solution was adjusted back to neutral using nitric acid and YSZ powder (d_{50} = 0.3 μm, TZ-8Y, Tosoh, Japan) was then slowly added while mixing. The pH was again readjusted to between pH 7–8 with nitric acid and LSM powder (d_{50} = 0.8 μm, LSM20-P, NexTech Materials, Lewis Center, OH) was slowly added under continued mixing and heavy sonication (S-450 A, Branson Ultrasonics, Danbury, CT). After the LSM powder had been completely dispersed (approximately 10 min of sonication), 5 wt.% (of the solids) of a polyethylene glycol (PEG) binder (Union Carbide Inc., Danbury, CT) was added into the suspension.[3] The ratio of LSM to YSZ was kept at a constant 40:60 vol.%.

Slurries were frozen using a copper-cooling rod attached to a liquid nitrogen reservoir. The freezing temperature was monitored and controlled using a PID Controller (CN7800, Omega, Stamford, CT) with a heating sleeve and thermocouple placed around the copper-cooling rod near the freezing surface. Dynamic freezing profiles, using linearly decreasing freezing temperatures, were used to promote approximately constant-sized ice lamellae and ceramic walls along the length of the freeze-casts.[19–21]

Before freezing, slurries were placed in a vacuum desiccator to remove any dissolved air. Slurries were then poured into cylindrical acrylic molds approximately 17 mm in diameter and 25 mm tall that had been attached with vacuum grease to the copper-cooling finger. Liquid nitrogen was added in combination with applied heat from the PID-controlled heating sleeve to linearly decrease the temperature of the copper rod at a controlled rate of 5 °C/min while the top of the mold remained open to ambient conditions. After complete solidification, the castings were freeze-dried (FreeZone 1L, Labconco, Kansas City, MO) for a minimum of 12 h. The green bodies were carefully removed from their molds and then partially sintered by heating to 450 °C at 2 °C/min, holding for 30 min and then to either 1200 °C (Sample A) or 1300 °C (Sample B) at 5 °C/min with a 2 h dwell time (CM Rapid TEMP Furnace, Bloomfield, NJ). The two sintering temperatures produced samples with approximately the same size of aligned macro-pores but with differing micro-pore morphologies (Fig. 2).

At the low sintering temperature (Fig. 2c), individual particles are easily distinguished, the structure appears rough and highly porous. In contrast, at the higher sintering temperature (Fig. 2d), individual particles can no longer be discerned, the overall structure appears to have coarsened and the micro-porosity is significantly reduced.

2.3. Microstructural analysis

In the literature, it has been observed that LSM and YSZ may react together under appropriate conditions to form the $La_2Zr_2O_7$ phase which is detrimental to electrode performance due to its low conductivity.[22,23] To establish whether or not this phase is present within the composite material, X-Ray Diffraction (XRD) patterns were taken of sintered LSM–YSZ freeze-casts that had been crushed into a fine powder. Diffractograms were taken with an X'Pert Pro MPD diffractometer (PANalytical Company) with Bragg-Brentano Geometry and Copper $K\alpha$ wavelength of 1.5418 Å. The patterns were indexed using the EVA software database.

To validate the spatial dispersion of both the LSM and YSZ within the porous composite, elemental mapping was performed on representative samples. Mapping was done using SEM (JSM-7000F, JEOL-USA, Inc., Peabody, MA) coupled with EDS.

A dual column FIB (Ga-ion) – field-emission gun scanning electron microscope (FEG-SEM NVISION 40, Carl ZEISS) with a 54° angle between the columns was used for FIB-SEM tomography. Before imaging, samples were infiltrated with a low viscosity resin (EpoHeat, Buehler, Irvine, CA) and mechanically

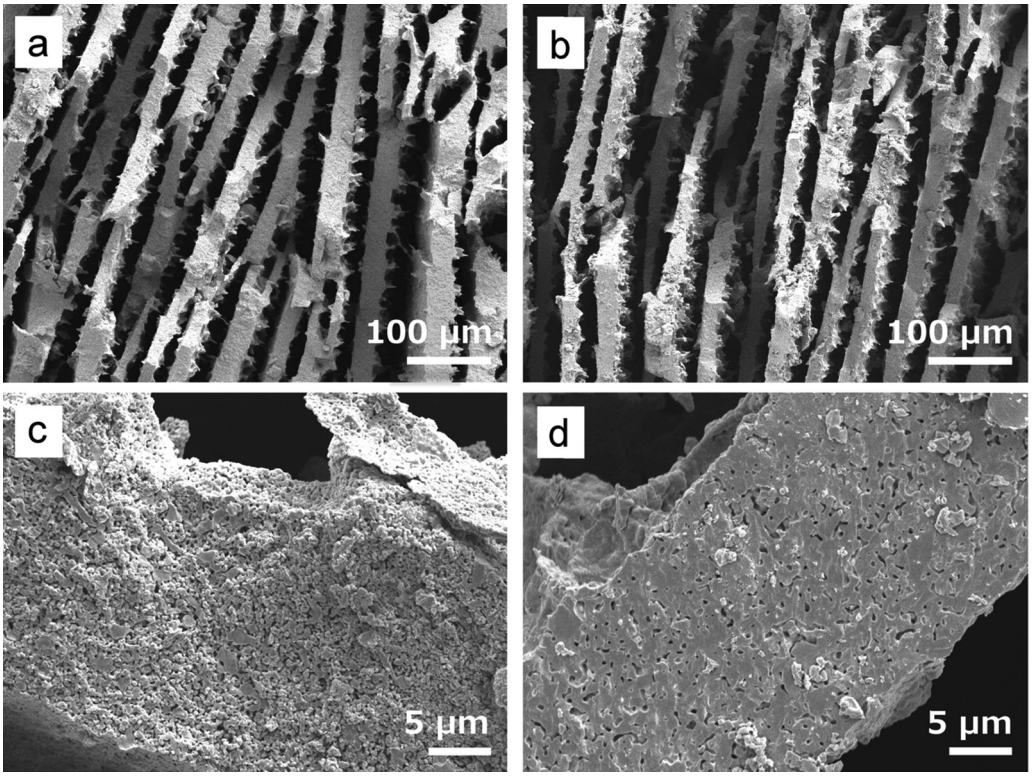

Fig. 2. Overview (a and b) and magnified (c and d) SEM micrographs of 23 vol.% composite LSM-YSZ freeze-casts frozen at 5 °C/min and sintered at (a and c) 1200 °C (Sample A) and (b and d) 1300 °C (Sample B) showing only small differences in macro-pore structure at the two different sintering temperatures but significant changes in ceramic wall microstructures.

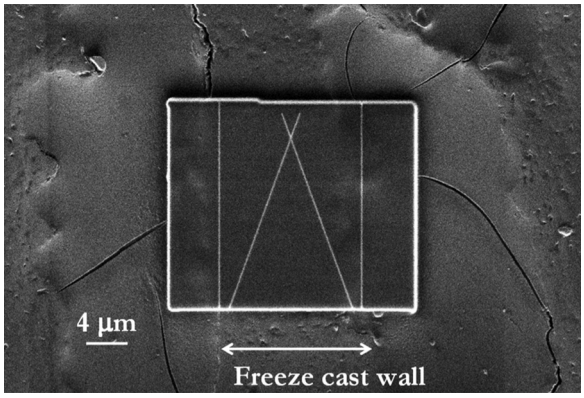

Fig. 3. Plan-view of the carbon coating and short-milled lines used to confirm FIB step size after imaging took place.

polished to a "mirror" finish. This improved contrast between the pore, LSM and YSZ phases. A carbon coating, 1 µm thick, which covered the entire thickness of a single ceramic lamella, was applied to the sample while in the microscope. Two lines at an angle of 40° from one another were then short-milled into the carbon layer. These lines served as a reference for post-confirming the FIB step size in the milling direction between successive images (Fig. 3). Post-calculations ensured that the average step size corresponded with the target value of 20 nm with only minor variations less than 2 nm.

After adding the reference lines, the volume surrounding the region of interest was milled away using the FIB gun so that a planar cross-section of the ceramic wall was presented. Two types of images (2048 × 1536 pixels) were then taken simultaneously: secondary electron (SE) images were used to reveal any pores which were possibly unfilled by resin and backscatter electron (BSE) images were recorded to differentiate LSM from YSZ (Fig. 4). After both images were acquired, a 20 nm slice was taken off from sample and another set of images was recorded of this newly exposed surface. This procedure was repeated until stacks of SE and BSE images of the desired sample volume were acquired.

2.4. Image processing, segmentation and analysis

Both stacks of raw grayscale images were first aligned using the Stackreg ImageJ plugin[24] to correct for a slight thermal drift. Then a median filter was applied to reduce the noise and improve the subsequent segmentation of the selected region of interest. Each phase was first segmented independently using a single threshold value and then several morphological operations (erosion and/or dilation) were applied to eliminate artifacts caused by the thresholding operation so that a good visual match was obtained with the initial grayscale image. For the high sintering temperature sample (Sample B), a non-negligible fraction of the porosity is closed and thus unfilled by the resin. The contrast between the unfilled pores and LSM or YSZ was not sufficient on the BSE images for good segmentation (Fig. 4b). To overcome this issue, the SE images were used to segment the pore phase on this sample (Fig. 4a). The three-segmented images

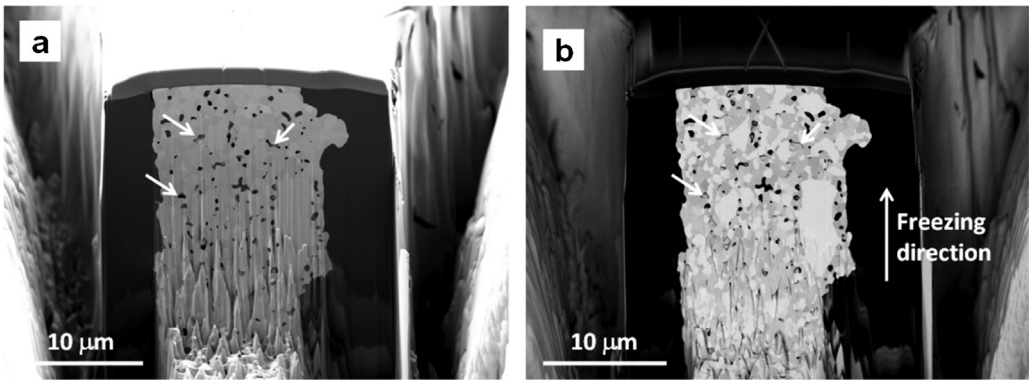

Fig. 4. (a) SE image and (b) BSE image of a section of sample B (sintered at 1300 °C). In the BSE image, infiltrated resin appears black, YSZ in medium gray and LSM in light gray. Pores appear black on the SE image even if unfilled by resin while they are only poorly visible on the BSE image (arrows).

were then combined into a single image with three levels of gray corresponding to the three different phases (Fig. 5).

The LSM:YSZ ratios extracted from the 3D segmented images (Table 1) compare favorably with the expected value of 40:60, which validates the segmentation process. The micro-porosity values are also reported in Table 1 but due to the hierarchical character of the porosity, no experimental value is available to compare with. However, the effect of sintering temperature on the micro-pore volume is clear.

Each phase has been geometrically analyzed in terms of size distribution, connectivity and TPB density using image analysis. A classical granulometry analysis with successive morphological erosions allows the size distribution of each phase to be obtained.[25,26]

In order to be electrochemically active, a TPB line should be connected to the three percolating networks for gas conduction (open porosity), ionic conduction (YSZ) and electronic conduction (LSM). To determine if a TPB line is active or inactive, the connectivity of its corresponding phase network must first be analyzed for each voxel. A connectivity value (connected, unconnected or unknown) is assigned to each voxel depending on its connection to the overall percolating networks. As the full electrode could not be imaged, assumptions were made for the connectivity of the faces of the 3D volume (Fig. 6).

The 1-1 faces of the sample are assumed to be connected to gas channels on both sides and therefore, unconnected to the ionic and electronic conductor networks. The 2-2 faces represent either the electrolyte or current collector and are assumed connected for ions and electrons but unknown for gas since there may be unconnected pores above and/or below the sampled volume. The connectivity of the 3-3 faces is assumed unknown for the porous, electronic and ionic phases since the sampled volume's location along the *z*-axis is unknown relative to the ends of the ceramic walls.

TPB density is computed using a voxel edge detection algorithm.[10,27,28] The values presented are corrected by a factor of 1.455 to account for the steps due to the voxel discretization, as proposed by Wilson et al.[10] TPBs are counted as active if all three phases (pore, LSM and YSZ) are connected.

2.5. Calculation of Tortuosity

In addition to determining phase connectivity, simulations were performed to obtain tortuosity factors for each phase (electronic/ionic conducting and pores). The effective diffusivity was calculated for the segmented 3D images by solving the Laplace equation (Eq. (1)) with the GeoDict software package.[29]

$$\Delta C_i = 0 \tag{1}$$

where C_i is the concentration of the species i which can be either an ion, electron or gas molecule. Periodic conditions were used assuming mirror symmetry along the three orthogonal directions

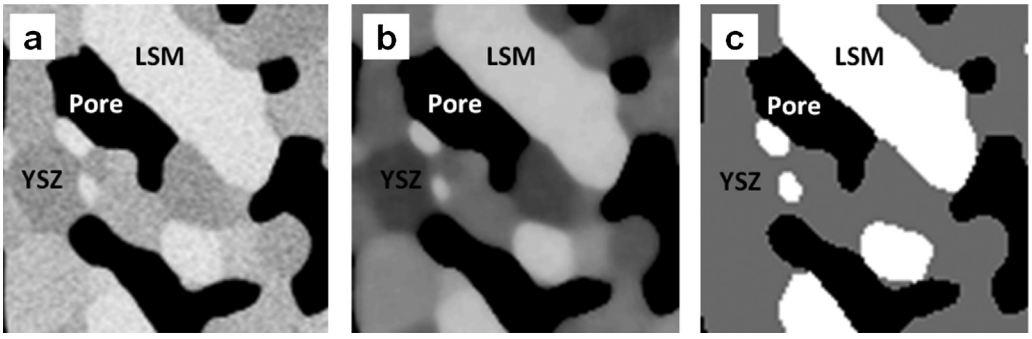

Fig. 5. Image processing. (a) Raw gray-scale BSE image (b) Image after median filtering (c) Final segmented image.

Table 1
FIB-SEM samples.

	Sintering temperature (°C)	Sample size (μm)	LSM/YSZ ratio	Microporosity (vol.%)
Sample A	1200	16.2 × 7.4 × 9.1	42.1/57.9	25.0
Sample B	1300	10.5 × 7.2 × 9.7	41.6/58.4	14.9

in the microstructure. The tortuosity τ in a direction k (either x, y, or z) is then calculated as:

$$\tau_k = \frac{\varphi D_{\text{int}}^{\text{o}}}{D_{\text{k}}^{\text{eff}}} \quad (2)$$

where $D_{\text{int}}^{\text{o}}$ is the intrinsic diffusivity of a species in its correspondent phase and φ represents the volume fraction of the considered phase. This intrinsic diffusivity is normalized by the effective diffusivity $D_{\text{k}}^{\text{eff}}$ in the tested tortuous porous structure.[30,31]

3. Results

3.1. Microstructural analysis

XRD of LSM–YSZ samples sintered at 1300 °C and then ground into powder show that the diffractogram can be indexed by only two phases, YSZ ($Y_{0.19}Zr_{0.81}O_{1.91}$) and LSM ($La_{0.8}Sr_{0.2}MnO_3$). There is no indication of the $La_2Zr_2O_7$ phase. Since there was no appreciable reactivity between LSM and YSZ at the higher sintering temperature, it is safe to assume that both samples A and B are free of the $La_2Zr_2O_7$ phase.

Looking at the microstructure itself, the procedure developed for co-dispersing and subsequently freeze-casting LSM–YSZ results in visually homogenous distributions of the LSM and YSZ phases (Fig. 7). Elemental mapping shows no significant segregation of the phases within the microstructure indicating good percolation of the electron and ion-conducting phases. FIB-SEM results are then used to determine phase dispersion at the scale of individual particles.

FIB-SEM 3D reconstructions for both the 1200 °C (Samples A) and 1300 °C (Sample B) show a homogenous distributions of the LSM and YSZ phases (Fig. 8). Sample B however exhibits a coarser microstructure with less microporosity than Sample A (14.9 vol.% versus 25 vol.%).

To quantitatively analyze the coarsening of the microstructure at the higher sintering temperature, the size distribution of each phase is computed through image analysis and is plotted in Fig. 9. These data confirm that the reconstructed volumes are good representative samples since the smallest dimensions of each reconstructed volume (7.4 and 7.2 μm) are 12 and 10 times larger, respectively, than the largest average particle size (LSM).[32] Secondly, it is observed that the average size of the LSM particles remains approximately the same when sintering temperature increased from 1200 °C to 1300 °C (800 nm and 740 nm, respectively), whereas the average size of the YSZ particles grows from 300 nm to 550 nm after sintering to 1300 °C. In addition, it should be noted that at the higher sintering temperature, the cumulative volume fraction of the pores decreases from 25 to 14.9 vol.%.

The various phase connectivity results are reported in Fig. 10. It is observed that all phases are nearly fully connected except for the pore phase in the sample sintered at 1300 °C, which shows a significant amount of unconnected and unknown connectivity volume. To avoid dealing with volumes of unknown connectivity, it is possible to apportion them into connected and unconnected phases using the connected/unconnected phase ratio from porosity values with known connectivity. For sample B, this process results in 62% of the total porosity being connected which is believed to be a more realistic value than the 35%

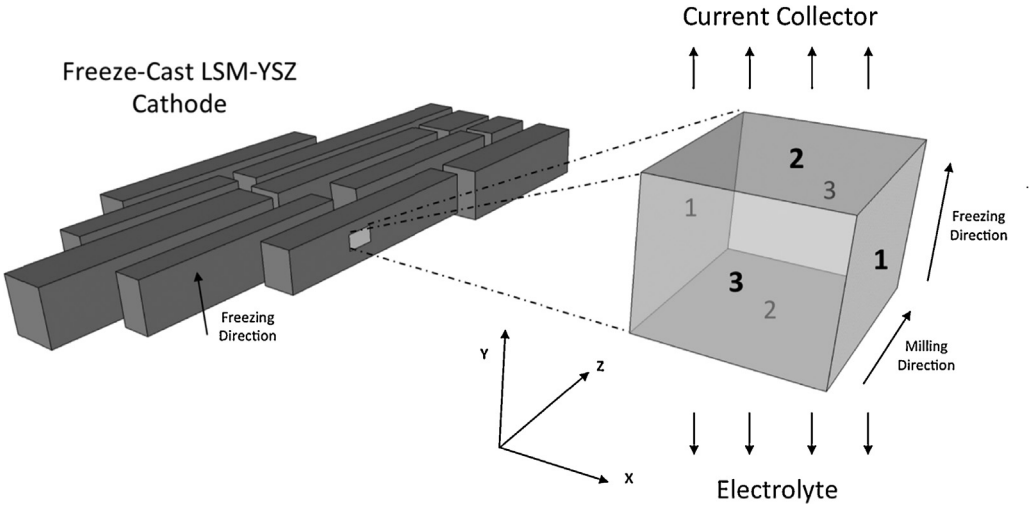

Fig. 6. Schematic of FIB-SEM sample and orientation of faces relative to the greater microstructure. The 1-1 faces are parallel to macro-pore gas channels. The 2-2 faces are perpendicular to the freezing direction and therefore connected to the entire LSM-YSZ conduction network and the 3-3 faces are assumed to have unknown connectivity. Both the electrolyte and current collector would presumably be applied normal to the freezing direction.

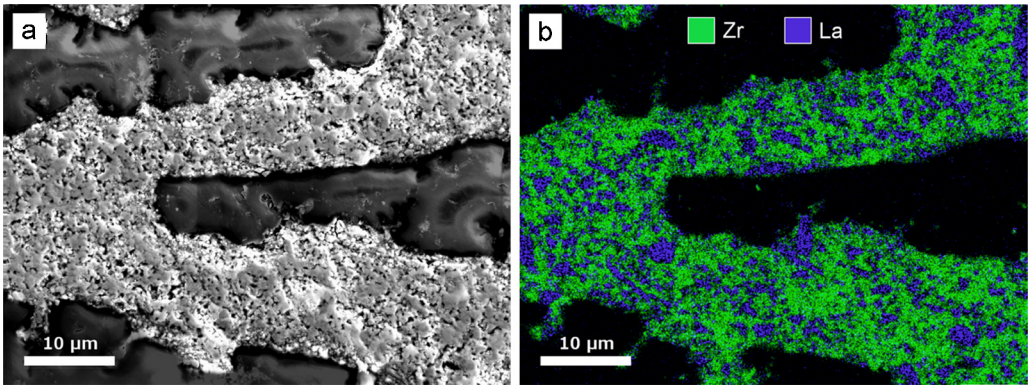

Fig. 7. (a) SEM image of freeze-cast walls and macro pores sintered at 1200 °C. (b) EDS map of Zirconia (green) and Lanthanum (blue) showing the spatial distribution of LSM and YSZ particles across two freeze-cast walls. The macro pores of the sample have been infiltrated with an epoxy resin (black regions) for sample preparation. The freezing direction is normal to the image.

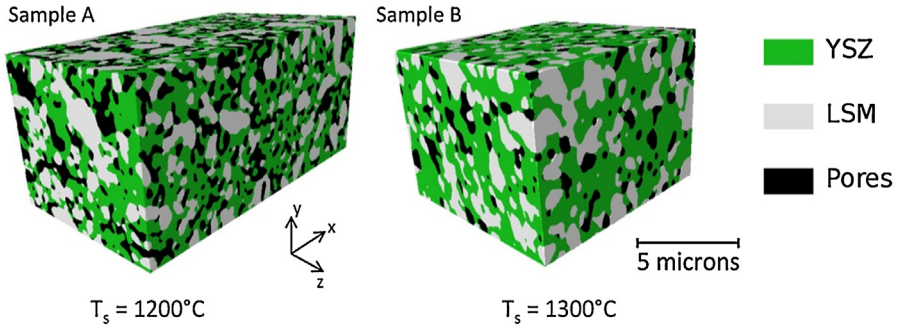

Fig. 8. 3D views of Samples A and B (1080 and 730 µm^3, respectively). The y-direction corresponds to the freezing direction and the z-direction to the milling direction. Note the clear coarsening behavior that occurs at the higher sintering temperature.

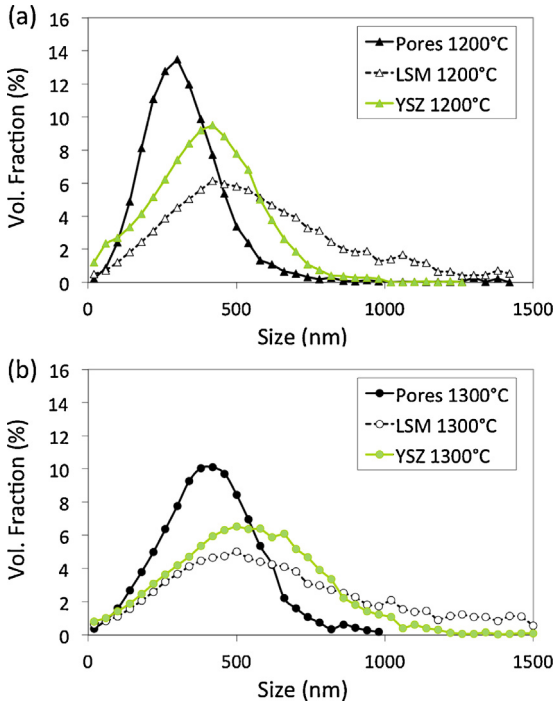

Fig. 9. Size distribution of the three phases. (a) Low sintering temperature (1200 °C) (b) High sintering temperature (1300 °C).

value obtained without counting the pore phase with unknown connectivity.

For electrochemical performance, proper quantitative accounting of the TPBs is important. TPB densities for each sample are determined using a similar approach for connectivity: TPBs with active, inactive and unknown statuses are first determined and then the unknown TPBs are apportioned between active and inactive, following the method described above. The results, reported in Fig. 11, show that sintering to the higher temperature significantly decreases the total TPB density as well as the proportion of TPBs that are active.

3.2. Calculated tortuosity

Using the quantitative microstructure, the tortuosity factors in the three spatial directions are calculated for the LSM, YSZ and pore phases and are plotted in Fig. 12. The relevant tortuosity direction for the conducting phases (LSM and YSZ) is the *y*-direction (freezing direction), which corresponds to the direction of current flow between the electrolyte and the current collector. The *x*-direction is relevant for gas flow through the pore phase. Computations in all directions however are of interest as they can provide some insight into the potential anisotropic nature of the microstructure at the scale of a single ceramic lamella.

For the YSZ and pore phases, the differences between the *x*, *y* and *z*-directions are negligible for both samples A and B, demonstrating the isotropy of these phases. For the LSM phase,

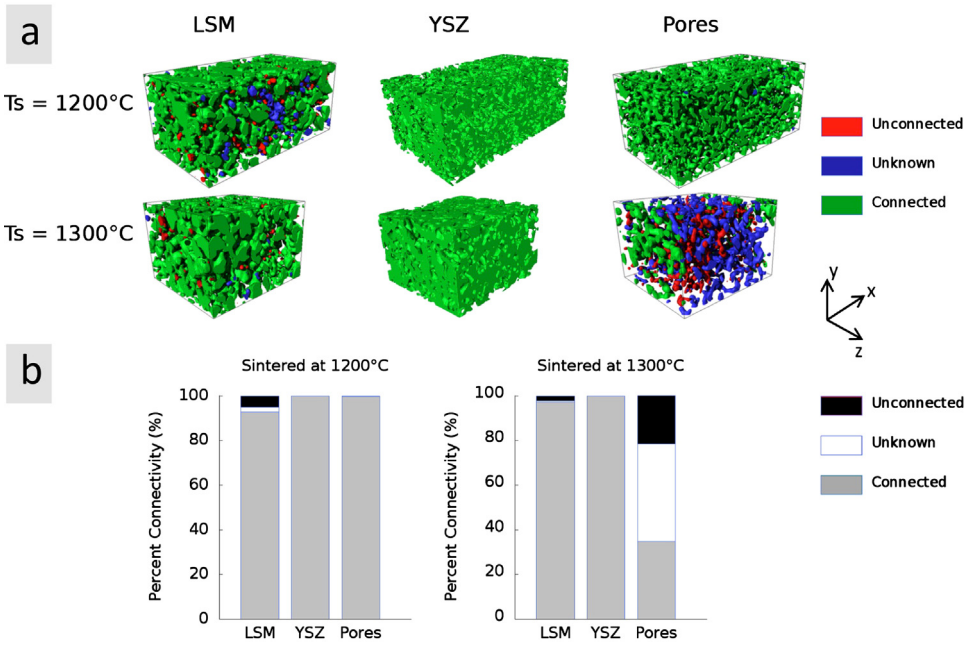

Fig. 10. (a) 3D representations of the phase connectivity of the various phases within the LSM-YSZ cathode. At the higher sintering temperature, the LSM increases its connectivity while the pore phases becomes markedly less connected. The YSZ phase is fully connected for both samples and appears to coarsen at the higher sintering temperature. (b) Phase connectivity in terms of volume fraction of the phases.

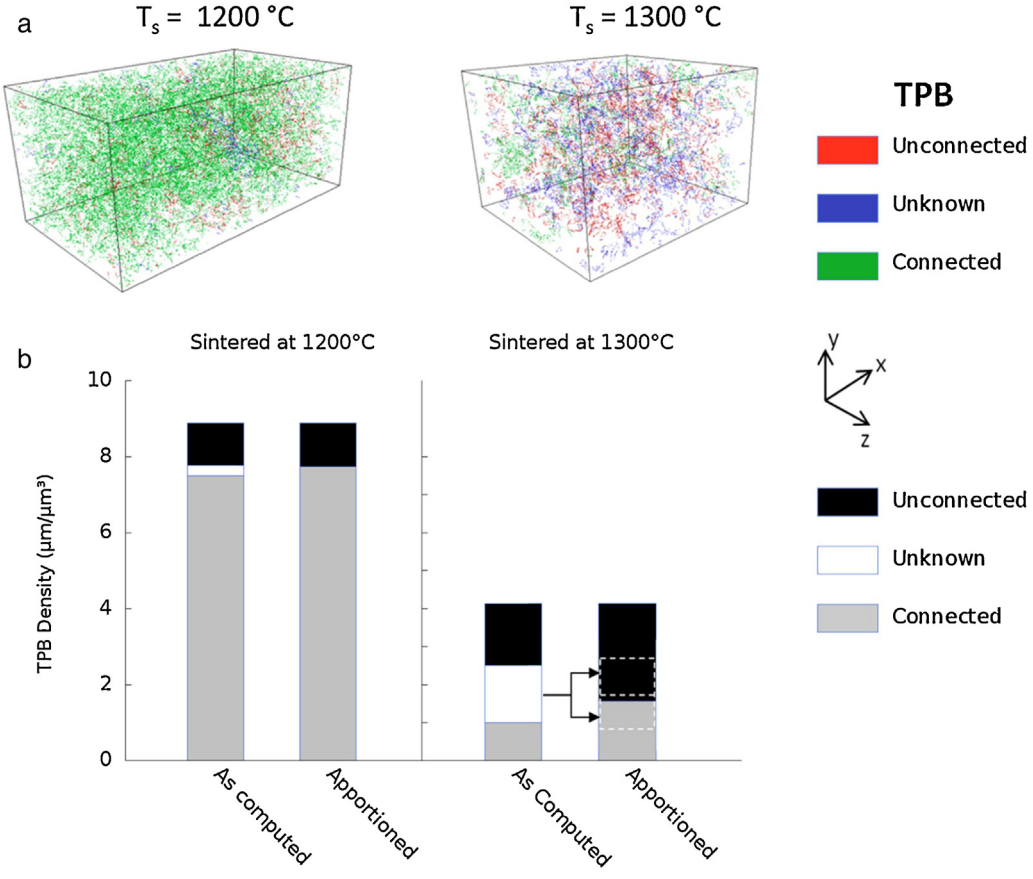

Fig. 11. (a) 3D representation of TPB density and connectivity within the tested sample volumes at 1200 and 1300 °C. (b) Computed TPB length from the reconstructed samples. For each sample, the first bar includes the TPB length with unknown connectivity and the second bar shows the final apportioned connectivity results with a consistent repartition of the unknown TPBs between active and inactive.

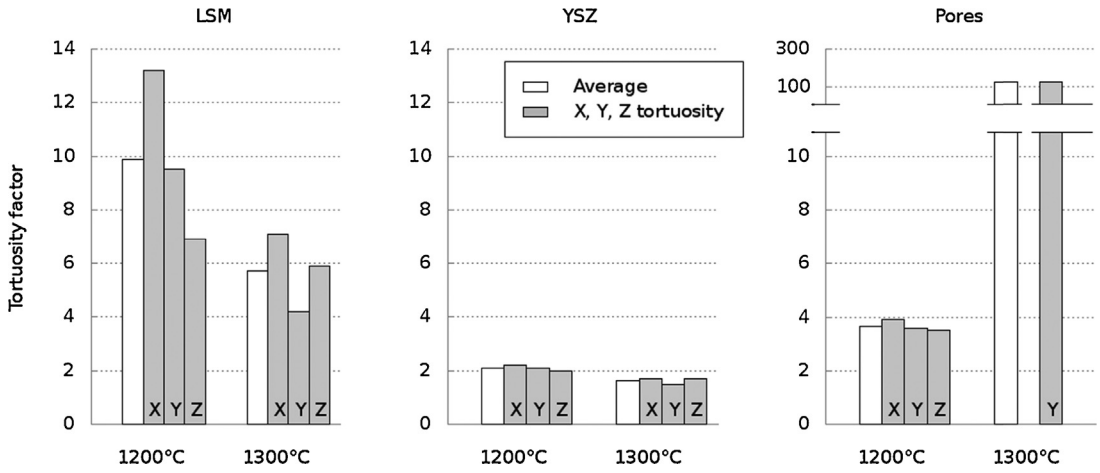

Fig. 12. Tortuosity factors for the LSM, YSZ and pore phases. The first bar of each group (white) shows the average tortuosity value for the three computed directions x (perpendicular to ceramic wall), y (freezing direction) and z (milling direction). For the samples sintered at 1300 °C, there is no percolation of porosity in the x and z directions therefore the tortuosity factor is infinite and not represented.

the tortuosity differences in the three directions are more pronounced but lack a clear trend, making it difficult to conclude on any possible phase-related anisotropy. Also, because the LSM particles are larger than the YSZ, the variations in LSM tortuosity may be partially attributed to the relatively small number of LSM particles in the representative volume. Generally however, tortuosity calculations show a decrease in tortuosity for both the ionic and electronic phases at the higher sintering temperature that can be attributed to coarsening of the structure. The pore phase however experiences a dramatic increase in tortuosity at the higher temperature due to the loss of porosity due to densification. For samples sintered at 1300 °C, the porosity is no longer connected in the x and the z directions resulting in infinite tortuosity.

4. Discussion

The qualitative and quantitative analysis of the FIB-SEM tomography data show that a high sintering temperature (1300 °C) decreases the freeze-cast microporosity from 25 vol.% (at 1200 °C) to 14.9 vol.% also leading to a significant degree of unconnected porosity (38 vol.% of the total micropore volume). Additionally, sintering to the higher temperature leads to an increase in grain size of the YSZ from 300 nm to 550 nm while preserving the size of the LSM grains. Overall, there is a decrease in the total TPB density as well as the active proportion of those TPBs. Due to densification however, tortuosity decreases by 40% for the LSM phase while at the same time tortuosity increases 100-fold for the pore phase. The tortuosity of the YSZ phase decreases only slightly at the higher sintering temperature. It should be emphasized that unconnected porosity is undesirable for the cathodes since it does not contribute to enhancing electrochemical activity while decreasing the mechanical properties.

The significant growth of the YSZ grains will negatively affect the TPB length and nullify the TPB gain expected from using fine starting powders. Grain coarsening is, however, generally difficult to avoid during high temperature sintering. It is worth noting that Cronin et al. observed significant grain growth for both LSM and YSZ.[33] They used significantly smaller starting particles for LSM, which could explain why they observed grain growth for LSM while we do not.

The first direct consequence of the presence of unconnected porosity within Sample B is the decrease in the active portion of the TPBs, from nearly 100% to 38%. This comes in addition to a significant decrease in the total (active and inactive) TPB length (from 8.9 $\mu m/\mu m^3$ to 4.1 $\mu m/\mu m^3$) due to YSZ particle coarsening and neck growth. However, as observed in Figs. 10 and 11, the connected porosity and active TPBs for Sample B are localized on the sides of the ceramic lamella, within a thickness of approximately 2 μm from the wall-edges. This seems to indicate that the presence of the aligned macro-pore channels allows for some active TPBs even with a microporosity value as low as 14.9%. In addition, decreasing the thickness of the lamella would improve the amount of connected pores and active TPBs. Thinner lamella can be achieved using faster freezing rates during freeze-casting.

While higher sintering temperatures result in reductions to TPB density and open porosity, the significant decrease in tortuosity also leads to increased conductivity for both the LSM and YSZ phases. While LSM conductivity is generally not a limiting factor for SOFC performance, due to the high intrinsic electronic conductivity of this material at operating temperatures, it is not the case for the low ionic conductivity of the YSZ phase that is primarily responsible for ohmic losses. Ohmic losses limit cell performance, and the TPB length taken alone is not necessarily the best indicator of electrochemical performance. An optimal microstructure results from a trade-off between activation and ohmic losses. For example, the maximum TPB length is obtained for a 50:50 LSM:YSZ ratio while the optimal ratio for cell performance is 40:60 when accounting for ohmic losses.[9,34]

Our analysis indicates that if our material system were to be used for a conventional isotropic composite LSM:YSZ cathode, the optimal sintering temperature would be approximately 1200 °C, which is in agreement with Cronin et al.[33] Sintering at higher temperatures reduces performance because of the low

activation due to unconnected porosity. However, the use of a lamellar, freeze-cast structure increases the active TPB density at low microporosity values thanks to the aligned gas channels. The optimal trade-off between activation and ohmic losses is therefore believed to shift toward higher sintering temperatures, which have the added benefit of strengthening the electrode. However, it is noted that the optimal sintering temperature may also depend on the average lamella thickness. After sintering to 1300 °C a large amount of the active TPBs are found within the zone approximately 2 μm from the gas channels while the TPBs in the core of the lamella are inactive (Fig. 11, Sample B). Thus, reducing the lamellar size could reduce the inactive core region and increase the density of active TPBs. Using a thin lamellar structure, it is believed that sintering temperatures as high as 1300 °C could be used without compromising the density of TPBs in order to increase the ionic conductivity.

5. Conclusions

A method for co-dispersing and freeze-casting aqueous suspensions of LSM and YSZ produces samples with a homogenous distribution of phases and fully percolating networks of ion- and electron-conducting particles has been developed and is reported here. FIB-SEM tomography shows that sintering to 1300 °C results in significant coarsening of the YSZ phase and decreased microporosity, but a negligible effect on the LSM phase. Additionally, the coarsened microstructure suffers from a loss in overall TPB density as well as a reduction in the activated proportion of those TPBs. Tortuosity calculations show that densification during sintering results in reductions in tortuosity for the solid phases (LSM and YSZ) but significant increases for the porous phase. However, the lamellar structure appears to localize activated TPBs near the lamellar surfaces, indicating that the optimal sintering temperature depends on the lamella size and may be shifted higher as compared to a standard isotropic electrode microstructure.

Acknowledgements

This research has been supported by the National Science Foundation under Grant No. DMR 1008600 and l'Agence Nationale de la Recherche under Grant No. 2010 BLAM 0931 01 as a Materials World Network Project.

References

1. Wincewicz KC, Cooper JS. Taxonomies of SOFC material and manufacturing alternatives. *J Power Sources* 2005;**140**:280–96.
2. Deville S. Freeze-casting of porous ceramics: a review of current achievements and issues. *Adv Eng Mater* 2008;**10**:155–69.
3. Deville S, Saiz E, Nalla RK, Tomsia AP. Freezing as a path to build complex composites. *Science* 2006;**311**:515–8.
4. Cable TL, Sofie SW. A symmetrical, planar SOFC design for NASA's high specific power density requirements. *J Power Sources* 2007;**174**:1–11.
5. Chen Y, Bunch J, Li T, Mao Z, Chen F. Novel functionally graded acicular electrode for solid oxide cells fabricated by the freeze-tape-casting process. *J Power Sources* 2012;**213**:93–9.
6. Moon J, Hwang H, Awano M, Maeda K. Preparation of NiO–YSZ tubular support with radially aligned pore channels. *Mater Lett* 2003;**57**:1428–34.
7. Lichtner AZ, Jauffrès D, Martin CL, Bordia RK. Processing of hierarchical and anisotropic porosity LSM–YSZ composites. *J Am Ceram Soc* 2013;**96**:2745–53.
8. Sunde S. Monte Carlo simulations of polarization resistance of composite electrodes for solid oxide fuel cells. *J Electrochem Soc* 1996;**143**:1930–9.
9. Schneider LCR, Martin CL, Bultel Y, Bouvard D, Seibert E, Siebert E. Discrete modelling of the electrochemical performance of SOFC electrodes. *Electrochim Acta* 2006;**52**:314–24.
10. Wilson JR, Cronin JS, Duong AT, Rukes S, Chen H-Y, Thornton K, Mumm DR, Barnett S. Effect of composition of ($La_{0.8}Sr_{0.2}MnO_3$–Y_2O_3-stabilized ZrO_2) cathodes: correlating three-dimensional microstructure and polarization resistance. *J Power Sources* 2010;**195**:1829–40.
11. Wilson JR, Cronin JS, Barnett SA. Linking the microstructure, performance and durability of Ni-yttria-stabilized zirconia solid oxide fuel cell anodes using three-dimensional focused ion beam–scanning electron microscopy imaging. *Scr Mater* 2011;**65**:67–72.
12. Cronin JS, Muangnapoh K, Patterson Z, Yakal-Kremski KJ, Barnett SA. Firing temperature effect on 3D microstructure and performance of LSM-YSZ composite SOFC cathodes. In: *219th ECS Meeting*. 2011.
13. Duong AT, Mumm DR. Microstructural optimization by tailoring particle sizes for LSM-YSZ solid oxide fuel cell composite cathodes. *J Electrochem Soc* 2012;**159**:B40–53.
14. Gannon P, Sofie S, Deibert M, Smith R, Gorokhovsky V. Thin film YSZ coatings on functionally graded freeze cast NiO/YSZ SOFC anode supports. *J Appl Electrochem* 2008;**39**:497–502.
15. Fisher ML, Colic M, Rao MP, Lange FF. Effect of silica nanoparticle size on the stability of alumina/silica suspensions. *J Am Ceram Soc* 2001;**84**:713–8.
16. Kakade MB, Das D, Ramanathan S. Studies on slip casting behavior of lanthanum strontium manganite. *Ceram Int* 2011;**37**:1789–93.
17. Hanifi AR, Zazulak M, Etsell TH, Sarkar P. Effects of calcination and milling on surface properties, rheological behaviour and microstructure of 8mol% yttria-stabilised zirconia (8 YSZ). *Powder Technol* 2012;**231**:35–43.
18. Snijkers F, de Wilde A, Nullens S, Luyten J. Aqueous tape casting of yttria stabilised zirconia using natural product binder. *J Eur Ceram Soc* 2004;**24**:1107–10.
19. Waschkies T, Oberacker R, Hoffmann MJ. Control of lamellae spacing during freeze casting of ceramics using double-side cooling as a novel processing route. *J Am Ceram Soc* 2009;**92**:S79–84.
20. Preiss A, Su B, Collins S, Simpson D. Tailored graded pore structure in zirconia toughened alumina ceramics using double-side cooling freeze casting. *J Eur Ceram Soc* 2012;**32**:1575–83.
21. Waschkies T, Oberacker R, Hoffmann MJ. Investigation of structure formation during freeze-casting from very slow to very fast solidification velocities. *Acta Mater* 2011;**59**:5135–45.
22. Kleveland K, Einarsud M-A, Schmidt CS, Shamsili S, Faaland S, Wiik K, Grande T. Reactions between strontium-substituted lanthanum manganite and yttria-stabilized zirconia: Part II. Diffusion couples. *J Am Ceram Soc* 1999;**82**:729–34.
23. Li N, Mahapatra MK, Singh P. Sintering of porous strontium doped lanthanum manganite-yttria stabilized zirconia composite in controlled oxygen atmosphere at 1400 °C. *J Power Sources* 2013;**221**:57–63.
24. Thévenaz P, Ruttimann UE, Unser M. A pyramid approach to subpixel registration based on intensity. *IEEE Trans Image Process* 1998;**7**:27–41.
25. Sweeney S, Martin C. Pore size distributions calculated from 3-D images of DEM-simulated powder compacts. *Acta Mater* 2003;**51**:3635–49.
26. Boulos V, Salvo L, Fristot V, Lhuissier P, Houzet D. Investigating performance variations of an optimized GPU-ported granulometry algorithm. In: *18th International European Conference on Parallel and Distributed Computing*. 2012.
27. Vivet N, Chupin S, Estrade E, Richard A, Bonnamy S, Rochais D, Bruneton E. Effect of Ni content in SOFC Ni-YSZ cermets: a three-dimensional study by FIB-SEM tomography. *J Power Sources* 2011;**196**:9989–97.
28. Grew KN, Peracchio Aa, Joshi AS, Izzo Jr JR, Chiu WKS. Characterization and analysis methods for the examination of the heterogeneous solid oxide fuel cell electrode microstructure: Part 1. Volumetric measurements of the heterogeneous structure. *J Power Sources* 2010;**195**:7930–42.
29. Geodict.com. *ConductoDict Tutorial ConductoDict Tutorial Documentation*; 2013.

30. Wilson JR, Kobsiriphat W, Mendoza R, Chen H-Y, Hiller JM, Miller DJ, Thornton K, Voorhees PW, Adler SB, Barnett SA. Three-dimensional reconstruction of a solid-oxide fuel-cell anode. *Nat Mater* 2006;**5**:541–4.
31. Becker J, Wieser C, Fell S, Steiner K. A multi-scale approach to material modeling of fuel cell diffusion media. *J Heat Mass Transfer* 2011;**54**:1360–8.
32. Joos J, Ender M, Carraro T, Weber A, Ivers-Tiffée E. Representative volume element size for accurate solid oxide fuel cell cathode reconstructions from focused ion beam tomography data. *Electrochim Acta* 2012;**3**:268–76.
33. Cronin JS, Muangnapoh K, Patterson Z, Yakal-Kremski KJ, Dravid VP, Barnett SA. Effect of firing temperature on LSM-YSZ composite cathodes: a combined three-dimensional microstructure and impedance spectroscopy study. *J Electrochem Soc* 2012;**159**:B385.
34. Völker B, McMeeking RM. Impact of particle size ratio and volume fraction on effective material parameters and performance in solid oxide fuel cell electrodes. *J Power Sources* 2012;**215**:199–215.